Journal Pre-proofs

Achieving enhanced thermoelectric performance of $Ca_{1-x-y}La_xSr_yMnO_3$ *via* synergistic carrier concentration optimization and chemical bond engineering

Taoyi Liu, Jie Chen, Meng Li, Guang Han, Can Liu, Dali Zhou, Jin Zou, Zhi-Gang Chen, Lei Yang

Please cite this article as: T. Liu, J. Chen, M. Li, G. Han, C. Liu, D. Zhou, J. Zou, Z-G. Chen, L. Yang, Achieving enhanced thermoelectric performance of $Ca_{1-x-y}La_xSr_yMnO_3$ *via* synergistic carrier concentration optimization and chemical bond engineering, *Chemical Engineering Journal* (2020), doi: https://doi.org/10.1016/j.cej.2020.127364

Achieving enhanced thermoelectric performance of $Ca_{1-x-y}La_xSr_yMnO_3$ *via* synergistic carrier concentration optimization and chemical bond engineering

Taoyi Liu[a], Jie Chen[a], Meng Li[b], Guang Han[c], Can Liu[a], Dali Zhou[a]*, Jin Zou[b,d], Zhi-Gang Chen[e], Lei Yang[a]*

[a] School of Materials Science and Engineering, Sichuan University, Chengdu, 610064, China

[b] School of Mechanical and Mining Engineering, The University of Queensland, Brisbane, Queensland, 4072, Australia

[c] College of Materials Science and Engineering, Chongqing University, Chongqing 400044, China

[d] Centre for Microscopy and Microanalysis, The University of Queensland, Brisbane, Queensland, 4072, Australia

[e] Centre for Future Materials, University of Southern Queensland, Springfield Central, Queensland 4300, Australia

Corresponding authors:

Lei Yang, Email: lyang1986@scu.edu.cn

Dali Zhou, Email: zdl@scu.edu.cn

Abstract

In this work, we fabricate perovskite-type $Ca_{1-x-y}La_xSr_yMnO_3$ thermoelectric materials using co-precipitation method, followed by cold pressing and hot sintering. The La/Sr dual doping modifies chemical composition and bonding properties of $CaMnO_3$, resulting in improved electrical transport properties with tunable carrier concentration, carrier mobility and effective mass. Meanwhile, the phonon transport properties are also influenced, reflected by the reduced lattice thermal conductivity of $Ca_{1-x-y}La_xSr_yMnO_3$. As a result, $Ca_{0.94}La_{0.02}Sr_{0.04}MnO_3$ shows significantly enhanced power factor up to 374 $\mu W \cdot m^{-1} \cdot K^{-2}$ and figure of merit up to ~0.22 at 973 K, which is ~144% higher than those of pristine $CaMnO_3$. This study rationalizes a potential strategy to improve the thermoelectric performance of $CaMnO_3$-based materials.

Key words: $CaMnO_3$; thermoelectric; dual doping; chemical bond engineering

1. Introduction

The increasing consumption of fossil fuels and the deteriorating environmental pollution have driven researchers to explore alternative and sustainable energy-supply technologies [1-3]. Thermoelectric materials and devices enable the direct conversion between heat and electricity [4], showing great potential in improving energy efficiency and recovering waste heat from diverse heat sources. Their conversion efficiency is dominated by the dimensionless figure-of-merit (zT) [5-8], defined as $zT = S^2\sigma T/\kappa$, where S, σ, κ and T are the Seebeck coefficient, electrical conductivity, thermal conductivity and absolute temperature, respectively. Accordingly, an ideal thermoelectric material relies on a large power factor ($PF = S^2\sigma$) and a low κ, while PF and κ are strongly coupled by the carrier concentration (n).

Currently, thermoelectric materials with zT values exceeding 1 have been extensively obtained [3, 9-15]. However, the high cost, instability in air atmosphere or toxicity may limit their applications [16-18]. Oxides-based thermoelectric ceramics with advantages of chemical and structural stability, low cost and low toxicity have been regarded as potential thermoelectric materials for applications above 800 K [19, 20]. As one of the promising candidates, n-type perovskite $CaMnO_3$ with intrinsically high $|S|$ (550 µV K^{-1} at room temperature) has received much interest due to its unique structure, magnetic and topological properties [21-30]. However, its high electrical resistivity (ρ) and κ lead to low zT values. Previous studies have revealed that the substitutions of trivalent rare earth elements such as La, Ce or Pr on the Ca-site of $CaMnO_3$ can simultaneously reduce ρ and κ, along with a moderate decrease of $|S|$ [31-

33]. Moreover, theoretical calculations [34, 35] indicate that Sr-doping can contribute to larger effective mass of carriers (m^*), enhanced density of states (DOS) near the Fermi level, and complicated phonon frequency modes, which is essential to optimize the thermoelectric parameters of $CaMnO_3$. Therefore, applying a dual doping strategy of rare earth elements and Sr on $CaMnO_3$ could be a key to achieve synergistically improved thermoelectric properties.

In this work, based on co-precipitation, cold pressing and hot sintering methods, we obtained significantly enhanced zT of $CaMnO_3$ by dual doping La/Sr on Ca^{2+} sites to increase PF and reduce the lattice thermal conductivity (κ_l), and an in-depth understanding of how these dopants affect the thermoelectric transport properties has been achieved by combining experimental analyses and first-principles calculations. It is confirmed that La doping can effectively increase n, and an optimized PF can be obtained at 973 K in $Ca_{0.98}La_{0.02}MnO_3$. Introducing Sr into $Ca_{0.98}La_{0.02}MnO_3$ can manipulate n, therefore, increase σ along with moderately decreased S, leading to further increased PF. The decoupling of electrical transport properties is mainly attributed to the increased carrier effective mass (m^*) and carrier mobility (μ) via modifying the chemical bonds and electrical band structure. Additionally, the dual doping of La/Sr could enhance the phonon scattering, decreasing κ_l of $CaMnO_3$. Ultimately, a zT of 0.22 at 973 K is achieved in $Ca_{0.94}La_{0.02}Sr_{0.04}MnO_3$, which is 144% higher than that of pristine $CaMnO_3$.

2. Methods

2.1 Experimental methods

Polycrystalline $Ca_{1-x-y}La_xSr_yMnO_3$ precursor powders were prepared by a chemical co-precipitation method. All starting materials in analytical grade were purchased from Kelong Chemical Co. Ltd (Chengdu) without any further purification. Specifically, 0.05 mol $MnCl_2 \cdot 4H_2O$ (99.7%), varied amounts of $CaCl_2$ (99.7%), $SrCl_2 \cdot 6H_2O$ (99.7%), and $La(NO_3)_3 \cdot 6H_2O$ (99.7%), were dissolved in 200 ml deionized water with stoichiometric ratios (for achieving $Ca_{1-x-y}La_xSr_yMnO_3$). Then 0.5 mol L^{-1} Na_2CO_3 (99.8%) aqueous solution as the precipitant were added to the mixed solutions in drops until the pH value reached 8. Those solutions were continuously stirred at 353 K for 2 h until Ca^{2+}, Sr^{2+}, Mn^{2+} and La^{3+} ions had been completely precipitated. The precipitate was dried in air at 393 K and then manually ground, followed by a calcine process in a Muffle furnace at 1173 K for 12 hours to obtain $Ca_{1-x-y}La_xSr_yMnO_3$ powders. Then all as-synthesized powder samples were cold-pressed into 15 mm diameter pellets under a pressure of 70 MPa and then sintered in a Muffle furnace at 1573 K for 12 h. The density d of the as-sintered pellets was measured by the Archimedes method. The theoretical density of a specific composition was calculated by the formula $d_{theo} = 4M \, NA^{-1} \, V^{-1}$, where M, NA and V are the molecular weight ($g \cdot mol^{-1}$), the Avogadro's constant (6.02×10^{23} mol^{-1}) and the cell volume from Rietveld analysis (cm^{-3}), respectively. The M are calculated based on the compositions of $Ca_{1-x-y}La_xSr_yMnO_3$, and the according values of cell volume (V) are obtained from XRD Rietveld refinement results. Thus, relative density (d_{rel}) is determined by $d_{rel} = d/d_{theo} \times 100\%$.

Powder X-ray diffraction (XRD) analysis was carried out by a diffractometer

(XRD-6100, Shimadzu) with Cu-Kα radiation (λ = 0.15418 nm) over 20°-70°. X-ray photoelectron spectroscopy (XPS, Escalab 250Xi, Thermo Fisher Scientific) analysis was applied to study the bonding states of the samples. The morphologies of all samples were investigated by using field emission scanning electron microscopy (SEM, S-4800, Hitachi) attached with an Energy-dispersive X-ray spectroscopy (EDS).

The as-sintered pellets were cut into square sheets (~ 10 mm × 10 mm × 2 mm) for measuring the thermoelectric properties. All the thermoelectric properties were measured perpendicular to pressing direction. S and σ were measured on a commercial equipment (CTA-5, Cryoall) from 320 K to 973 K. The room-temperature Hall carrier concentration (n_{H}), Hall mobility (μ_{H}), Hall coefficient (R_{H}) were measured by Van der Pauw method (VDP6800, Sadhudesign) under a reversible magnetic field of 1.5 T. The thermal diffusivity (D) was evaluated by a laser flash method (LFA 457, Netzsch Instrument). The specific heat capacity (C_{p}) was estimated according to Dulong-Petit law, which can be described as $C_{\mathrm{p}}=3NR/M$, where N is the number of atoms per formula unit, M is the molecular weight and R is the universal gas constant (8.314 J mol^{-1} K^{-1}) [36]. κ was calculated by the equation $\kappa = DC_{\mathrm{p}}d$. The uncertainties of all measurements were less than 5%, and uncertainties of PF, κ and zT were less than 20%.

2.2 Computational methods

In this work, the calculations were based on G-type anti-ferromagnetic cells with orthorhombic symmetry. The 2 × 1 × 2 supercells (expansion of *Pnma* 5.3193 Å × 7.4148 Å × 5.2093 Å with α = β = γ = 90°), namely $Ca_4Mn_4O_{12}$ for $CaMnO_3$ and

$Ca_{14}LaSrMn_{16}O_{48}$ for $Ca_{0.88}La_{0.06}Sr_{0.06}MnO_3$, were first built and relaxed. Calculations with the projector augment wave (PAW) approach and generalized gradient approximations (GGA) based on density functional theory (DFT) was performed on the Vienna Ab-initio Simulation Package (VASP). The GGA in the form of Perdew-Burke-Ernzerhof (PBE) functional with the inclusion of the Hubbard energy item using the Liechtenstein approaches ($U = 2$ eV and $J = 1$ eV since the exchange interaction is poorly screened in solids [37, 38], as suggested by previous studies [39, 40]) for treating on-site Coulomb interactions on Mn d electrons were used for pseudo atomic calculation for Ca_sv, Sr_sv Mn_pv, O and La. The cutoff energy for plane wave expansion of the wave function was set at 350 eV. The convergence criteria for total energy calculation and ion relaxation of all the forces between atoms are 0.0001 eV and 0.01 eV/Å, respectively. For the density of states (DOS) calculation, Brillouin zone is sampled with $5 \times 3 \times 5$ Monkhorst-Pack grids.

3. Results and discussion

Fig. 1a and 1b show XRD patterns of as-synthesized $Ca_{1-x-y}La_xSr_yMnO_3$ powders and as-sintered bulk samples. All the XRD peaks can be well-indexed as the orthorhombic perovskite phase with *Pnma* space group (confirmed by PDF#89-0666), indicating that the $CaMnO_3$-based materials are successfully synthesized and there is no phase change after sintering. Table 1 summarizes the lattice parameters of all sintered samples from Rietveld refinement of XRD patterns in Fig. S1. As can be seen, substituting Ca by La and Sr almost linearly expands the *a*, *b*, and *c* values of $CaMnO_3$, because the ionic radii of both La^{3+} (1.216 Å) and Sr^{2+} (1.26 Å) are larger than that of Ca^{2+} (1.12 Å) [41].

The lattice parameter of c does not change monotonously because of acceptable fluctuations in XRD refinement calculations.
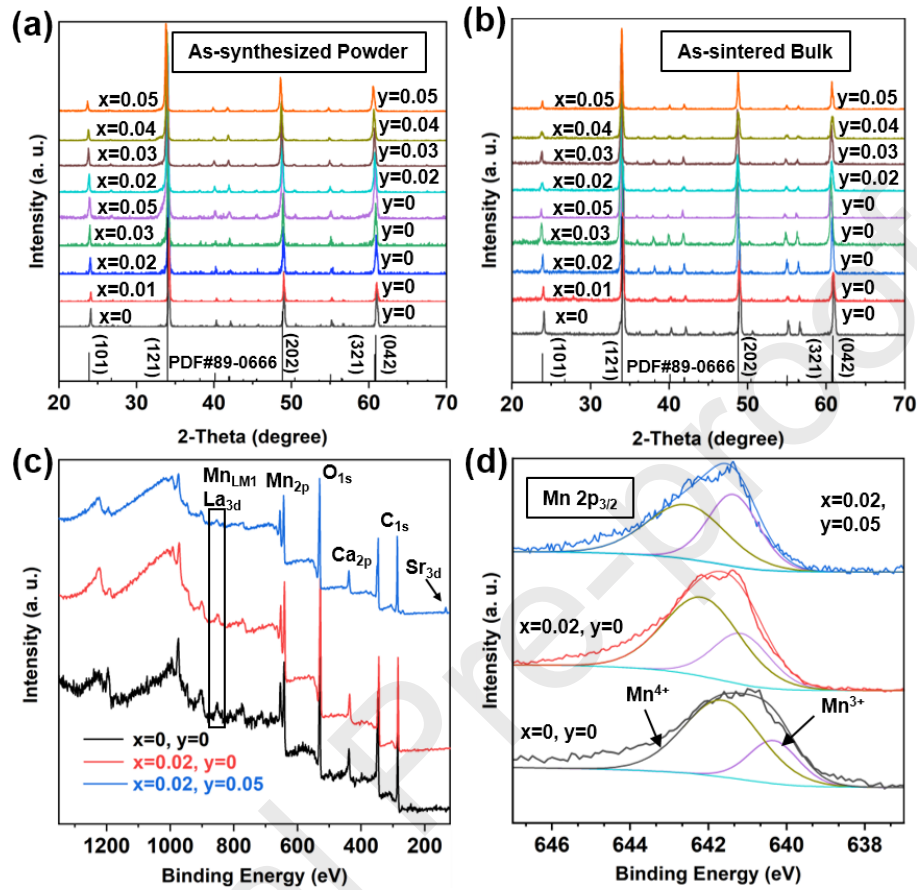

Fig. 1. XRD patterns of $Ca_{1-x-y}La_xSr_yMnO_3$ (a) as-synthesized powders and (b) as-sintered bulk samples. (c) XPS survey spectra and (d) high-resolution Mn $2p_{3/2}$ XPS spectra of $Ca_{1-x-y}La_xSr_yMnO_3$ (x = 0, y = 0; x = 0.02, y = 0; x = 0.02, y = 0.05).

To investigate the evolution of chemical compositions and bonding states after La and Sr doping, XPS survey and high-resolution scans of Mn $2p_{3/2}$ peaks of $Ca_{1-x-y}La_xSr_yMnO_3$ (x=0, y=0; x=0.02, y=0; x=0.02, y=0.05) were performed and the corresponding spectra are shown in Fig. 1c and 1d, respectively. From Fig. 1c, Mn 2p, O 1s and Ca 2p peaks are strong in all three samples, while La 3d peaks are difficult to

be observed because La 3d peaks overlap with Mn_{LM1} peaks, and Sr 3d peaks can be observed in $Ca_{0.93}La_{0.02}Sr_{0.05}MnO_3$. By comparing the relative areas of de-convoluted Mn 2p peaks (Fig. 1d), we can see that the valance states of Mn are clearly affected by the La and Sr doping, while Mn^{3+}/Mn^{4+} ratios in $CaMnO_3$, $Ca_{0.98}La_{0.02}MnO_3$ and $Ca_{0.93}La_{0.02}Sr_{0.05}MnO_3$ are calculated to be 0.40, 0.48 and 0.85, respectively. In other words, the partial substitution of Ca^{2+} by La^{3+}/Sr^{2+} can induce the conversion of Mn^{4+} into Mn^{3+}, which can enhance the transport of electrons by hopping mechanism [42]. The ionic radius of Sr^{2+} is larger than La^{3+}, leading to a relaxed structure distortion, which will significantly change the carrier concentration and carrier mobility (discussed later). Thus, further doping with isovalent Sr^{2+} influence the $Mn^{3+}/Mn4^{+}$ ratio more obviously than electron-donor doping.

Table 1. Lattice parameters and relative densities of $Ca_{1-x-y}La_xSr_yMnO_3$.

Sample ID		a (Å)	b (Å)	c (Å)	Volume	Relative
x	y				($Å^3$)	Density (%)
0	0	5.282	7.463	5.272	207.82	91.1
0.01	0	5.284	7.466	5.277	208.18	91.5
0.02	0	5.286	7.468	5.286	208.67	93.2
0.03	0	5.288	7.469	5.275	208.34	94.6
0.05	0	5.293	7.480	5.288	209.36	95.9
0.02	0.02	5.280	7.466	5.293	208.65	93.7
0.02	0.03	5.288	7.467	5.278	208.40	97.0
0.02	0.04	5.289	7.472	5.280	208.66	96.3
0.02	0.05	5.294	7.479	5.289	209.41	93.8

SEM were used to characterize as-synthesized powders and as-sintered bulks of $CaMnO_3$, $Ca_{0.98}La_{0.02}MnO_3$ and $Ca_{0.93}La_{0.02}Sr_{0.05}MnO_3$ and the results are presented in Fig. 2. As shown in Fig. 2a-c, the pristine $CaMnO_3$ powder shows uniformly distributed

particle-like morphology with an average particle size of ~1 μm, while the particles of $Ca_{0.02}La_{0.98}MnO_3$ and $Ca_{0.93}La_{0.02}Sr_{0.05}MnO_3$ have smaller sizes (< 0.5 μm), indicating that the addition of La can inhibit the growth of $CaMnO_3$ grains [43]. However, after hot sintering, all samples have similar grain sizes (Fig. S2). From Fig. 2d-f, all the as-sintered samples are well-densified with high relative densities (Table 1). The existence of La and Sr can be further confirmed by EDS profiles (insets of Fig. 2d and f, respectively), which suggests that the real chemical compositions are very close to the nominal compositions. Also, from the EDS elemental maps (Fig. 2g), La and Sr are uniformly distributed in $Ca_{0.92}La_{0.02}Sr_{0.05}MnO_3$.

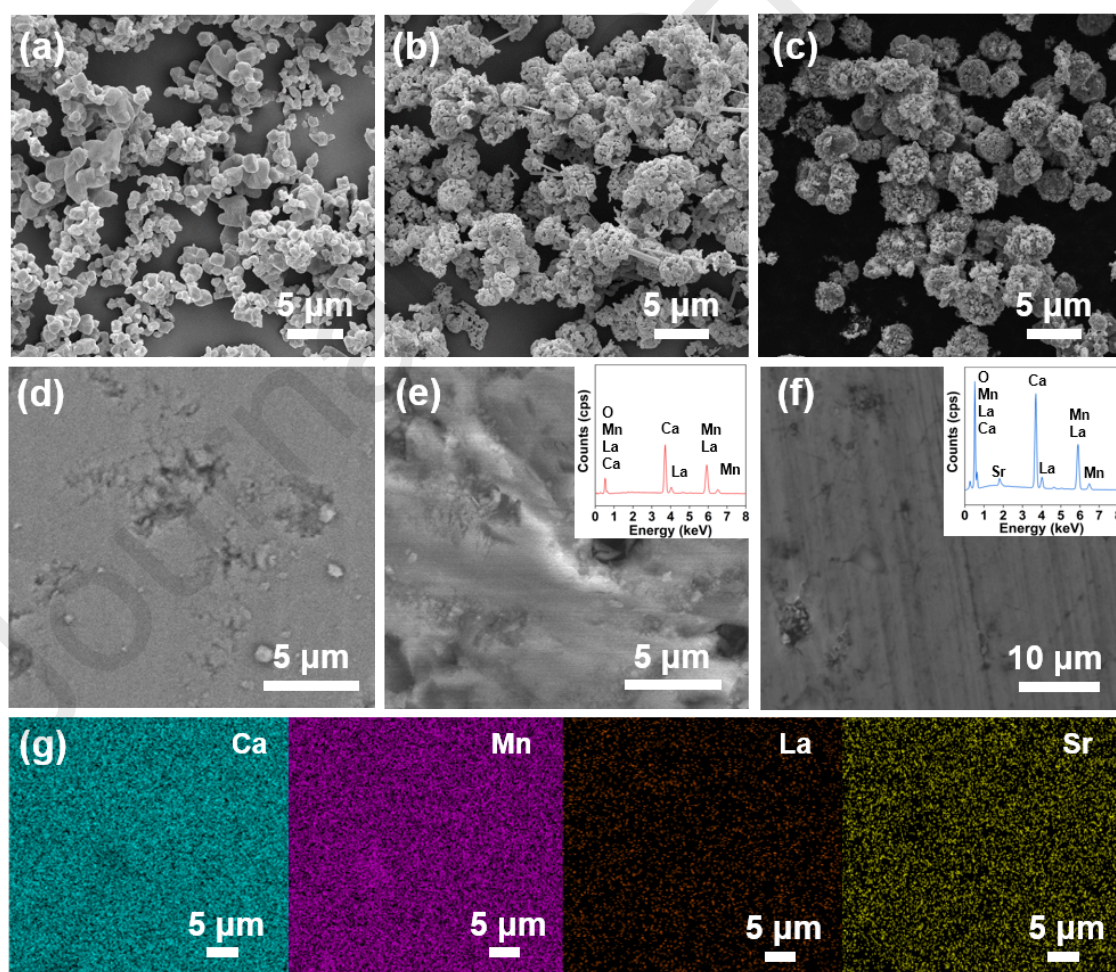**Fig. 2.** SEM images of as-synthesized (a) $CaMnO_3$, (b) $Ca_{0.98}La_{0.02}MnO_3$ and (c)

$Ca_{0.93}La_{0.02}Sr_{0.05}MnO_3$ powders; SEM images of polished as-sintered (d) $CaMnO_3$, (e) $Ca_{0.98}La_{0.02}MnO_3$ and (f) $Ca_{0.93}La_{0.02}Sr_{0.05}MnO_3$ bulks, the insets in (e) and (f) show the corresponding EDS profiles; (g) the corresponding EDS elemental maps of Ca, Mn, La and Sr from the same area in (f).

To theoretically examine the effects of La and Sr co-doping to the electrical transport properties of $CaMnO_3$, we calculated the partial density of states (PDOS) of intrinsic $CaMnO_3$ and $Ca_{0.88}La_{0.06}Sr_{0.06}MnO_3$. Fig. 3a illustrates the schematic supercell of $Ca_{14}LaSrMn_{16}O_{48}$ ($Ca_{0.88}La_{0.06}Sr_{0.06}MnO_3$), and the calculated PDOS of $CaMnO_3$ and $Ca_{14}LaSrMn_{16}O_{48}$ are plotted in Fig. 3b and c. As can be seen, $Ca_{0.88}La_{0.06}Sr_{0.06}MnO_3$ shows a metallic conductive behavior while intrinsic $CaMnO_3$ is semi-conductive. It should be noted that DOS near Fermi level of $Ca_{0.88}La_{0.06}Sr_{0.06}MnO_3$ is larger than that of pristine $CaMnO_3$, suggesting that La and Sr doped $CaMnO_3$ has heavier effective mass [44, 45]. These results indicate that La and Sr dual doped $CaMnO_3$ is expected to have enhanced electrical transport properties.
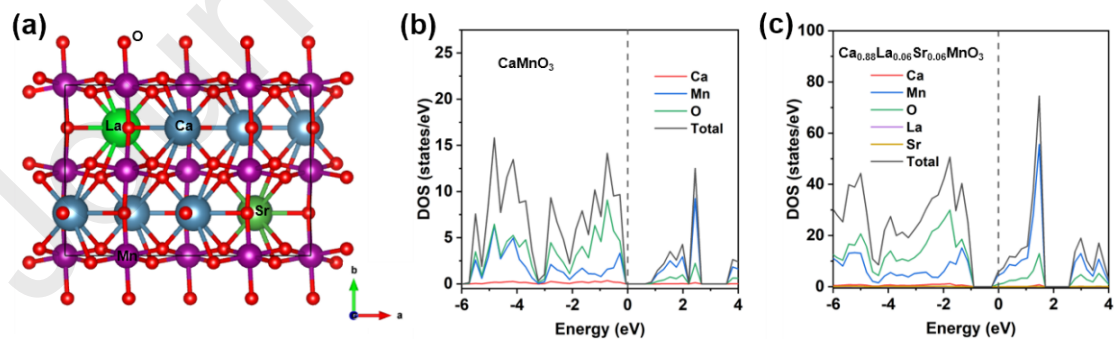

Fig. 3. (a) The super cell of orthorhombic $Ca_{0.88}La_{0.06}Sr_{0.06}MnO_3$, viewing from [001] direction; the PDOS of (b) $CaMnO_3$, (c) $Ca_{0.88}La_{0.06}Sr_{0.06}MnO_3$. The Fermi energy is set at 0 eV.

Fig. 4 plots temperature-dependent thermoelectric properties of $Ca_{1-x-y}La_xSr_yMnO_3$. As shown in Fig. 4a, σ of $Ca_{1-x-y}La_xSr_yMnO_3$ ($x \leq 0.02$, $y = 0$) increases with increasing the temperature, indicating the semi-conductive behavior ($d\sigma/dT > 0$), while the rest samples represent metallic conduction ($d\sigma/dT < 0$). This is because that the La/Sr dual doping leads to higher Mn^{3+}/Mn^{4+} ratios, and more electrons fill e_g orbitals, which can widen the e_g orbital to an itinerant band and then the transport behavior will become metallic-like [46]. σ of $Ca_{1-x}La_xMnO_3$ ($x \geq 0.02$) is markedly higher than that of the pristine $CaMnO_3$ (25.9 S·cm^{-1} at 973 K), which is mainly due to the increased n_H (Table S1) by trivalent La^{3+} doping. The substitution of La^{3+} for Ca^{2+} can provide large numbers of electrons, increasing the Mn^{3+}/Mn^{4+} ratio, and thus promote the hopping of electrons between Mn^{3+} and Mn^{4+} sites. In other words, free electrons are introduced into the e_g orbital to work as charge carriers in the Mn^{3+}-O-Mn^{4+} framework, leading to reduced ρ [33]. However, the metallic conductivity of $Ca_{1-x}La_xMnO_3$ ($x > 0.02$) induces reduced $|S|$ (Fig. 4b) and PF (Fig. 4c) at elevated temperature, indicating that the electrical properties of $Ca_{0.98}La_{0.02}MnO_3$ should be further optimized. To secure a good σ, Sr was introduced into $Ca_{0.98}La_{0.02}MnO_3$. Unlike La mono doping, doping Sr into $Ca_{1-x}La_xMnO_3$ ($x = 0.02$) not only increases n_H (Table 2), resulting in the conversion from semi-conductivity into metallic conductivity as discussed above, but also tunes the μ_H via relaxing the lattice distortion. In perovskite-type AMO_3 (M = 3d transition metals), M3d-O2p hybridization mainly determines the electronic structure around Fermi level, thereby affecting the electrical properties [47]. The dual doping of La^{3+}/Sr^{2+} in $CaMnO_3$ induces a structural distortion of the MnO_6 octahedron, altering

the Mn-O-Mn bond angles and the Mn-O bond lengths [48]. The degree of structural

distortion can be evaluated by the tolerance factor $t = (r_A+r_O)/[\sqrt{2} * (r_B+r_O)]$, where r_A,

r_B and r_O are the average ionic radii of A-site, B-site and O in perovskite ABO_3,

respectively [42]. In this study, ionic radii of Shannon ($r_{Ca^{2+}} = 1.12$ Å, $r_{La^{3+}} = 1.216$ Å,

$r_{Sr^{2+}} = 1.26$ Å, $r_{Mn^{4+}} = 0.53$ Å, $r_{O^{2-}} = 1.40$ Å) have been used [41]. With increasing the

Sr doping level, the t values of $Ca_{1-x-y}La_xSr_yMnO_3$ (x = 0.02, y = 0.02, 0.03, 0.04, 0.05)

are calculated to be 0.9250, 0.9255, 0.9260, 0.9265, respectively, indicating a relaxed

orthorhombic distortion [49]. In other words, the substitution of Ca^{2+} by Sr^{2+} relaxes

the bending of Mn-O-Mn bonds, widening the bandwidth of conduction band, leading

to a notably increased mobility of e_g electrons and a consequent increase of σ [48].

Increasing of Sr doping level can enhance the correlation of the $3d_{3z^2-r^2}$ orbital order

of Mn^{3+}, which reduces the number of the itinerant electrons [50]. Therefore,

optimizing the chemical bonds of Mn-O-Mn by Sr doping can strongly modify both n_H

and μ_H of $Ca_{1-x-y}La_xSr_yMnO_3$ (x = 0.02, y = 0.02, 0.03, 0.04, 0.05).

Fig. 4b shows the measured S of $Ca_{1-x-y}La_xSr_yMnO_3$. Negative values can be

observed from 323 K to 973 K, indicating the n-type nature of all samples. The $|S|$

values of $Ca_{1-x}La_xMnO_3$ gradually decrease with increasing La doping level. This is

attributed to the increased n_H, which is in good agreement with previous studies [31,

33, 43]. However, the $|S|$ values of $Ca_{1-x-y}La_xSr_yMnO_3$ (x = 0.02, y = 0.02, 0.03, 0.04,

0.05) exceed 230 μV K^{-1} in spite of their high n_H. To clarify the effect of Sr doping on

$|S|$, we estimated m^* using the following equations [51-53]:

$$S = -\frac{k_B}{e}\left(\frac{\left(s+\frac{5}{2}\right)F_{s+\frac{3}{2}}(\eta)}{\left(s+\frac{3}{2}\right)F_{s+\frac{1}{2}}(\eta)} - \eta\right) \tag{1}$$

$$F_s(\eta) = \int_0^\infty \frac{x^s}{1+e^{x-\eta}}dx \tag{2}$$

$$n = 4\pi\left(\frac{2m^*k_BT}{h^2}\right)^{3/2}F_{\frac{1}{2}}(\eta) \tag{3}$$

where k_B, e, s, F_s, η and h are the Boltzmann constant, the elementary electric charge, the scattering parameter, the Fermi integral, the reduced chemical potential and the Planck constant, respectively. Ionized impurity scattering ($s = 3/2$) was assumed to be dominant in the calculation [51]. Table 2 lists obtained m^*/m_0 values, from which m^* decreases with increasing Sr content, attributed to the lager bandwidth caused by relaxing the octahedral distortion of the $CaMnO_3$ [33, 51]. To further understand the relatively high $|S|$ values of the La/Sr dual-doped samples, we used $S = \frac{8\pi^2k_B}{3eh^2}m^*T\left(\frac{\pi}{3n}\right)^{2/3}$ [54] to describe S since the n_H ($> 10^{19}$ cm^{-3}) of our dual-doped samples are far larger than the estimated maximum critical concentration of degenerate $CaMnO_3$ ($n_c = 6.55 \times 10^{16}$ cm^{-3}) [55, 56]. It should be noted that S values are dominated by $m^*/n^{2/3}$ values while high σ largely depends on the weighed mobility $\mu(m^*)^{3/2}$ [45, 57]. A shown in Table 2, we can see that $m^*/n^{2/3}$ of $Ca_{0.94}La_{0.02}Sr_{0.04}MnO_3$ is comparable to that of $Ca_{0.98}La_{0.02}MnO_3$, while $\mu(m^*)^{3/2}$ of $Ca_{0.94}La_{0.02}Sr_{0.04}MnO_3$ is 83% higher than that of $Ca_{0.98}La_{0.02}MnO_3$. This means minimally decreased S and significantly enhanced PF can be obtained in $Ca_{0.94}La_{0.02}Sr_{0.04}MnO_3$, which has been

verified in the observed high *PF* value (347 µW·m^{-1}·K^{-2}) of Ca$_{0.94}$La$_{0.02}$Sr$_{0.04}$MnO$_3$ at
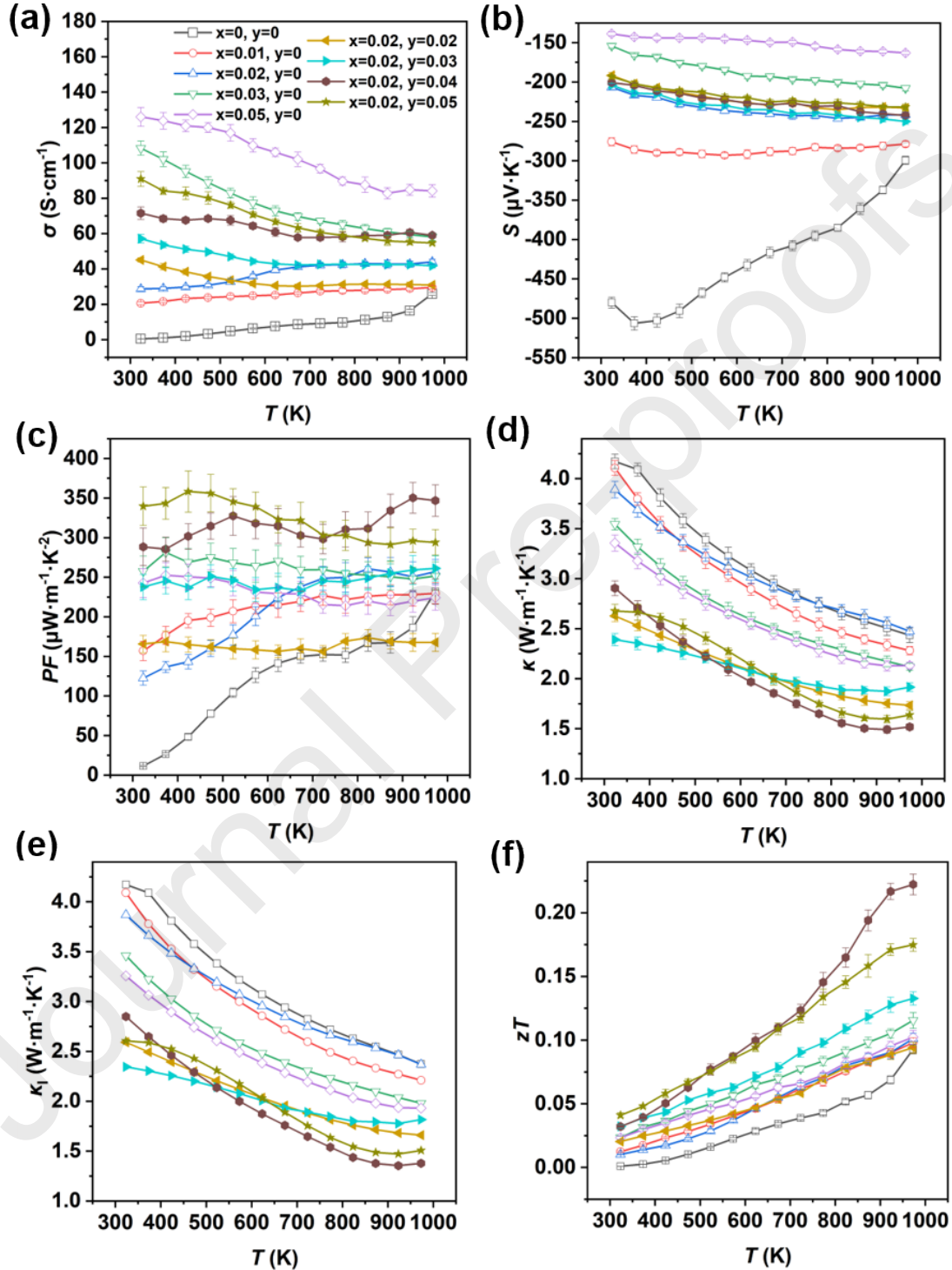
973 K.

Fig. 4. Temperature-dependent (a) electrical conductivity (σ), (b) Seebeck coefficient

(*S*), (c) power factor (*PF*), (d) total thermal conductivity (κ), (e) lattice thermal

conductivity (κ_l) and (f) figure of merit (zT) of $Ca_{1-x-y}La_xSr_yMnO_3$.

Table 2. The measured Hall concentration (n_H), Hall carrier mobility (μ_H), the calculated effective mass (m^*), $m^*/n^{2/3}$, and the weighed mobility ($\mu(m^*)^{3/2}$) at room temperature for $Ca_{1-x-y}La_xSr_yMnO_3$ (x = 0.02; y = 0, 0.02, 0.03, 0.04, 0.05) samples.

Sample ID		n_H	μ_H	m^* (m_0)	$m^*/n^{2/3}$	$\mu(m^*)^{3/2}$
x	y	(10^{20}/cm^3)	(cm^2/Vs)		($m_0 10^{-14}$ cm^2)	($m_0^{3/2}$cm^2/Vs)
0.02	0	0.85	2.08	0.87	4.50	1.69
0.02	0.02	1.54	1.67	1.15	4.00	2.06
0.02	0.03	1.25	2.33	1.10	4.40	2.69
0.02	0.04	0.92	3.72	0.88	4.32	3.07
0.02	0.05	0.88	5.35	0.80	4.04	3.83

κ can be expressed as the sum of κ_l and the electrical thermal conductivity (κ_e) as $\kappa = \kappa_l + \kappa_e$. According to the Wiedemann-Franz's law, $\kappa_e = L_0\sigma T$, where $L_0 = \pi^2 k_B 2/3e^2 = 2.45 \times 10^{-8}$ V^2·K^{-2} is the Lorentz constant [58]. On this basis, Fig. 4d and 4e plots the calculated κ and κ_l of $Ca_{1-x-y}La_xSr_yMnO_3$ (D was shown in Fig. S3a). As can be seen, κ declines gradually with increasing T and κ_l is the predominant component in κ since the contribution of κ_e to κ is less than 10%. With stronger phonon scattering induced by La doping, the κ_l values of $Ca_{1-x}La_xMnO_3$ decrease with the increasing La doping level, which is attributed to the enhanced crystallographic distortion and mass fluctuation strain [31, 59]. Further doping Sr into $Ca_{0.98}La_{0.02}MnO_3$ can introduce more point

defects that strongly scatter short-wavelength phonons, which overwhelms the relaxed lattice distortion, leading to reduced κ_l [48, 60]. Accordingly, $Ca_{0.94}La_{0.02}Sr_{0.04}MnO_3$ achieves a lowest κ_l of 1.38 $W \cdot m^{-1} \cdot K^{-1}$ at 973 K, which is reduced by 42% compared to that of pristine $CaMnO_3$.

Consequently, we have successfully modified n_H and chemical bonding structures *via* La/Sr dual doping in $CaMnO_3$. This strategy can optimize the electrical transport properties and introduce point defects to obtain high σ, large $|S|$ and low κ_l. Benefiting from the synergistically optimized thermoelectric parameters, a maximum zT of 0.22 at 973 K is obtained in $Ca_{0.94}La_{0.02}Sr_{0.04}MnO_3$, which shows good stability (Fig. S3b). This value is 120% and 144% higher than that of La-doped $Ca_{0.98}La_{0.02}MnO_3$ and pristine $CaMnO_3$ bulk, respectively (Fig. 4f). Also, such a synergistic strategy that combines carrier concentration optimization and chemical bond engineering leads to superior thermoelectric performance comparing to some other strategies [33, 48, 58, 61] involves La or Sr doping (Table S2).

4. Conclusion

In conclusion, we develop a synergistic La/Sr dual doping strategy to tune carrier concentration and chemical bonds of $CaMnO_3$-based thermoelectric materials. Our calculation and experimental results indicate that La/Sr dual doping can effectively relax the distortion of the MnO_6 octahedron and modify the band structure of $CaMnO_3$ to introduce electrons. In addition, La/Sr dual doping strengthens phonon scattering in $Ca_{1-x-y}La_xSr_yMnO_3$, which leads to reduced κ. Finally, a remarkably enhanced zT of

~0.22 is obtained in $Ca_{0.94}La_{0.02}Sr_{0.04}MnO_3$ at 973 K, which represents a 144% increasement than that of pristine $CaMnO_3$. Our study provides a feasible route to effectively control the carrier and phonon transport behavior for achieving high thermoelectric performance of $CaMnO_3$-based materials.

Declaration of Competing Interest

The authors declare that they have no known competing financial interests or personal relationships that could have appeared to influence the work reported in this paper.

References

[1] L. Yang, Z.G. Chen, M.S. Dargusch, Zou Jin, High performance thermoelectric materials: progress and their applications, Adv. Energy Mat. 8 (2018) 1701797.

[2] M. Hong, Z.G. Chen, L. Yang, J. Zou, $Bi_xSb_{2-x}Te_3$ nanoplates with enhanced thermoelectric performance due to sufficiently decoupled electronic transport properties and strong wide-frequency phonon scatterings, Nano Energy 20 (2016) 144-155.

[3] X.L. Shi, J. Zou, Z.G. Chen, Advanced thermoelectric design: from materials and structures to devices, Chem. Rev. (2020).

[4] Y.Z. Pei, X.Y. Shi, A. LaLonde, H. Wang, L.D. Chen, G.J. Snyder, Convergence of electronic bands for high performance bulk thermoelectrics, Nature 473 (2011) 66-69.

[5] J. He, T.M. Tritt, Advances in thermoelectric materials research: looking back and moving forward, Science 357 (2017) eaak9997.

[6] Z.G. Chen, G. Han, L. Yang, L.N. Cheng, J. Zou, Nanostructured thermoelectric materials: current research and future challenge, Prog. Nat. Sci. 22 (2012) 535-549.

[7] L. Huang, J.Z. Lu, D.W. Ma, C.M. Ma, B. Zhang, H.Y. Wang, G.Y. Wang, D.H. Gregory, X.Y. Zhou, G. Han, Facile in situ solution synthesis of SnSe/rGO nanocomposites with enhanced thermoelectric performance, Journal of Materials Chemistry A 8 (2020) 1394-1402.

[8] H.Y. Wang, X.F. Liu, B. Zhang, L. Huang, M.L. Yang, X. Zhang, H. Zhang, G.Y. Wang, X.Y. Zhou, G. Han, General surfactant-free synthesis of binary silver

chalcogenides with tuneable thermoelectric properties, Chem. Eng. J. 393 (2020) 124763.

[9] C. Chang, M.H. Wu, D.S. He, Y.L. Pei, C.F. Wu, X.F. Wu, H.L. Yu, F.Y. Zhu, K.D. Wang, Y. Chen, L. Huang, J.F. Li, J.Q. He, L.D. Zhao, 3D charge and 2D phonon transports leading to high out-of-plane ZT in n-type SnSe crystals, Science 360 (2018) 778-783.

[10] W. Li, L.L. Zheng, B.H. Ge, S.Q. Lin, X.Y. Zhang, Z.W. Chen, Y.J. Chang, Y.Z. Pei, Promoting SnTe as an eco-friendly solution for p-PbTe thermoelectric via band convergence and interstitial defects, Adv. Mater. 29 (2017) 1605887.

[11] M. Hong, Z.G. Chen, L. Yang, Y.C. Zou, M.S. Dargusch, H. Wang, J. Zou, Realizing zT of 2.3 in $Ge_{1-x-y}Sb_xIn_yTe$ via reducing the phase-transition temperature and introducing resonant energy doping, Adv. Mater. 30 (2018) 1705942.

[12] Y.C. Lan, A.J. Minnich, C. Gang, Z.F. Ren, Enhancement of thermoelectric figure-of-merit by a bulk nanostructuring approach, Adv. Funct. Mater. 20 (2010) 357-376.

[13] T. Zhu, Y. Liu, C. Fu, J.P. Heremans, J.G. Snyder, X. Zhao, Compromise and synergy in high-efficiency thermoelectric materials, Adv. Mater. 29 (2017) 1605884.

[14] G.J. Tan, L.D. Zhao, M.G. Kanatzidis, Rationally designing high-performance bulk thermoelectric materials, Chem. Rev. 116 (2016) 12123-12149.

[15] Y. Wang, W.D. Liu, X.L. Shi, M. Hong, L.J. Wang, M. Li, H. Wang, J. Zou, Z.G. Chen, Enhanced thermoelectric properties of nanostructured n-type Bi_2Te_3 by suppressing Te vacancy through non-equilibrium fast reaction, Chem. Eng. J. 391 (2020) 123513.

[16] D. Feng, Z.H. Ge, Y.X. Chen, J. Li, J.Q. He, Hydrothermal synthesis of SnQ (Q = Te, Se, S) and their thermoelectric properties, Nanotechnology 28 (2017) 455707.

[17] Y. Saiga, K. Suekuni, B. Du, T. Takabatake, Thermoelectric properties and structural instability of type-I clathrate $Ba_8Ga_{16}Sn_{30}$ at high temperatures, Solid State Commun. 152 (2012) 1902-1905.

[18] J. Mao, Z. Liu, J. Zhou, H. Zhu, Q. Zhang, G. Chen, Z. Ren, Advances in thermoelectrics, Adv. Phys. 67 (2018) 69-147.

[19] Y.N. Yin, B. Tudu, A. Tiwari, Recent advances in oxide thermoelectric materials and modules, Vacuum 146 (2017) 356-374.

[20] H. Ohta, K. Sugiura, K. Koumoto, Recent progress in oxide thermoelectric materials: p-type $Ca_3Co_4O_9$ and n-type $SrTiO_3$, Inorg. Chem. 47 (2008) 8429-8436.

[21] M. Matsukawa, A. Tamura, Y. Yamato, T. Kumagai, S. Nimori, R. Suryanarayanan, Thermal transport in electron-doped manganites $Ca_{1-x}Ce_xMnO_3$, J. Magn. Magn. Mater. 310 (2007) e283–e285.

[22] C.R. Wiebe, J.E. Greedan, J.S. Gardner, Z. Zeng, M. Greenblatt, Charge and magnetic ordering in the electron-doped magnetoresistive materials, Phys. Rev. B 64 (2001) 064421.

[23] R. Kabir, T.S. Zhang, D.Y. Wang, D. Richard, R.M. Tian, T.T. Thiam, S. Li, Improvement in the thermoelectric properties of $CaMnO_3$ perovskites by W doping, J. Mater. Sci. 49 (2014) 7522-7528.

[24] M. Schrade, R. Kabir, S. Li, T. Norby, T.G. Finstad, High temperature transport properties of thermoelectric $CaMnO_{3-\delta}$ — indication of strongly interacting small

polarons, J. Appl. Phys. 115 (2014) 103705-103705-103707.

[25] N.N. Loshkareva, L.V. Nomerovannaya, E.V. Mostovshchikova, A.A. Makhnev, L.N. Rybina, Electronic structure and polarons in $CaMnO_{3-\delta}$ single crystals: optical data, Phys. Rev. B 70 (2004) 155-163.

[26] R. Kabir, R.M. Tian, T.S. Zhang, R. Donelson, T.T. Tan, S. Li, Role of Bi doping in thermoelectric properties of $CaMnO_3$, J. Alloys Compd. 628 (2015) 347-351.

[27] F.P. Zhang, X. Zhang, Q.M. Lu, J.X. Zhang, Y.Q. Liu, Electronic structure and thermal properties of doped $CaMnO_3$ systems, J. Alloys Compd. 509 (2011) 4171-4175.

[28] F.P. Zhang, Q.M. Lu, X. Zhang, J.X. Zhang, First principle investigation of electronic structure of $CaMnO_3$ thermoelectric compound oxide, J. Alloys Compd. 509 (2011) 542-545.

[29] F.P. Zhang, Q.M. Lu, X. Zhang, J.X. Zhang, Electrical transport properties of $CaMnO_3$ thermoelectric compound: a theoretical study, Journal of Physics Chemistry of Solids 74 (2013) 1859-1864.

[30] F.P. Zhang, J.W. Zhang, J.X. Zhang, X.Y. Yang, X. Zhang, Effects of Sr doping on electronic and thermoelectrical transport properties of $CaMnO_3$ based oxide, Acta Physica Sinica 66 (2017) 247202.

[31] W. Yang, S. Yu, X.J. Wang, W.H. Su, Effects of substituting La^{3+}, Y^{3+} and Ce^{4+} for Ca^{2+} on the high temperature transport and thermoelectric properties of $CaMnO_3$, J. Phys. D-Appl. Phys. 42 (2009) 055010.

[32] F. Zhang, B. Niu, K. Zhang, X. Zhang, Q. Lu, J. Zhang, Effects of praseodymium doping on thermoelectric transport properties of $CaMnO_3$ compound system, J. Rare

Earths 31 (2013) 885-890.

[33] W. Yang, S. Yu, H.J. Fan, X.J. Wang, X.Y. Liu, High temperature thermoelectric response of electron-doped $CaMnO_3$, Chem. Mater. 21 (2009) 4653-4660.

[34] F.P. Zhang, X. Zhang, Q.M. Lu, J.X. Zhang, Y.Q. Liu, R.F. Fan, G.Z. Zhang, Doping induced electronic structure and estimated thermoelectric properties of $CaMnO_3$ system, Physica B 406 (2011) 1258-1262.

[35] F.P. Zhang, J.W. Zhang, J.X. Zhang, X.Y. Yang, X. Zhang, Effects of Sr doping on electronic and thermoelectrical transport properties of $CaMnO_3$ based oxide, Acta Physica Sinica 66 (2017) 247202.

[36] X. Tan, Y.C. Liu, K.R. Hu, G.K. Ren, Y.M. Li, L. Rui, Y.H. Lin, J.L. Lan, C.W. Nan, Synergistically optimizing electrical and thermal transport properties of Bi_2O_2Se ceramics by Te-substitution, J. Am. Ceram. Soc. 101 (2017) 326-333.

[37] E. Antonides, E.C. Janse, G.A. Sawatzky, LMM Auger spectra of Cu, Zn, Ga, and Ge, II. Relationship with the L23 photoelectron spectra via the L2L3M45 Coster-Kronig process, Phys. Rev. B 15 (1977) 5603.

[38] V.I. Anisimov, J. Zaanen, O.K. Andersen, Band Theory and Mott Insulators: Hubbard U Instead of Stoner I, Phys. Rev. B 44 (1991) 943-954.

[39] D.A. Tompsett, S.C. Parker, P.G. Bruce, M.S. Islam, Nanostructuring of β-MnO_2: The Important Role of Surface to Bulk Ion Migration, Chem. Mater. 25 (2013) 536-541.

[40] M. Molinari, D.A. Tompsett, S. Parker, F. Azough, R. Freer, Structural, Electronic and Thermoelectric Behaviour of $CaMnO_3$ and $CaMnO_{(3-\delta)}$, Journal of Materials

Chemistry A 2 (2014) 14109-14117.

[41] R.D. Shannon, Revised effective ionic radii and systematic studies of interatomic distances in halides and chalcogenides, Acta Cryst. 32 (1976) 751-767.

[42] Y. Wang, Y. Sui, J. Cheng, X. Wang, Z. Lu, W. Su, High temperature metal-insulator transition induced by rare-earth doping in perovskite $CaMnO_3$, J. Phys. Chem. C 113 (2009) 12509-12516.

[43] J. Lan, Y. Lin, M. Ao, C. Nan, L. Yong, B. Zhang, J. Li, High-temperature electric properties of polycrystalline La-doped $CaMnO_3$ ceramics, J. Mater. Sci. Technol. 025 (2009) 535-538.

[44] T. Okuda, K. Nakanishi, S. Miyasaka, Y. Tokura, Large thermoelectric response of metallic perovskites, Phys. Rev. B 63 (2001) 113104.

[45] J.L. Lan, Y.C. Liu, B. Zhan, Y.H. Lin, B.Q. Zhang, X. Yuan, W.Q. Zhang, W. Xu, C.W. Nan, Enhanced thermoelectric properties of Pb-doped BiCuSeO ceramics, Adv. Mater. 25 (2013) 5086-5090.

[46] Y. Wang, Y. Sui, W.H. Su, High temperature thermoelectric characteristics of $Ca_{0.9}R_{0.1}MnO_3$ (R=La, Pr, ... , Yb), J. Appl. Phys. 104 (2008) 1325.

[47] J.B. Torrance, P. Lacorre, A.I. Nazzal, E.J. Ansaldo, C. Niedermayer, Systematic study of insulator-metal transitions in perovskites $RNiO_3$ (R=Pr, Nd, Sm, Eu) due to closing of charge-transfer gap, Phys. Rev. B 45 (1992) 8209.

[48] A. Kosuga, Y. Isse, Y. Wang, K. Koumoto, R. Funahashi, High-temperature thermoelectric properties of $Ca_{0.9-x}Sr_xYb_{0.1}MnO_{3-\delta}$ (0≤x≤0.2), J. Appl. Phys. 105 (2009) 804.

[49] D. Flahaut, T. Mihara, R. Funahashi, N. Nabeshima, K. Lee, H. Ohta, K. Koumoto, Thermoelectrical properties of A-site substituted $Ca_{1-x}Re_xMnO_3$ system, J. Appl. Phys. 100 (2006) 084911.

[50] T. Okuda, Y. Fujii, Cosubstitution effect on the magnetic, transport, and thermoelectric properties of the electron-doped perovskite manganite $CaMnO_3$, J. Appl. Phys. 108 (2010) 103702.

[51] K. Iwasaki, T. Ito, T. Nagasaki, Y. Arita, M. Yoshino, T. Matsui, Thermoelectric properties of polycrystalline $La_{1-x}Sr_xCoO_3$, J. Solid State Chem. 181 (2008) 3145-3150.

[52] Y. Wang, Y. Sui, X. Wang, W. Su, X. Liu, Enhanced high temperature thermoelectric characteristics of transition metals doped $Ca_3Co_4O_{9+\delta}$ by cold high-pressure fabrication, J. Appl. Phys. 107 (2010) 42.

[53] M. Hong, Z.G. Chen, L. Yang, Z.M. Liao, Y.C. Zou, Y.H. Chen, S. Matsumura, J. Zou, Achieving zT > 2 in p-type $AgSbTe_{2-x}Se_x$ alloys via exploring the extra light valence band and introducing dense stacking faults, Adv. Energy Mat. (2017) 1702333.

[54] M. Cutler, J.F. Leavy, R.L. Fitzpatrick, Electronic transport in semimetallic cerium sulfide, Phys. Rev. 133 (1964) A1143-A1152.

[55] P.P. Edwards, Universality aspects of the metal-nonmetal transition in condensed media, Phys. Rev. B 17 (1978) 2575-2581.

[56] S. Bhattacharjee, E. Bousquet, P. Ghosez, First-principles study of the dielectric and dynamical properties of orthorhombic $CaMnO_3$, J. Phys.: Condens. Matter 20 (2008) 255229.

[57] Y.Z. Pei, A.D. Lalonde, H. Wang, G.J. Snyder, E. Science, Low effective mass

leading to high thermoelectric performance, Energy Environ. Sci. 5 (2012) 7963-7969.

[58] K.K. Liu, Z.Y. Liu, F.P. Zhang, J.X. Zhang, X.Y. Yang, J.W. Zhang, J.L. Shi, G. Ren, T.W. He, J.J. Duan, Improved thermoelectric performance in Pr and Sr co-doped $CaMnO_3$ materials, J. Alloys Compd. 808 (2019) 151476.

[59] J.S. Cha, D.H. Kim, H.Y. Hong, G.H. Kim, K. Park, Effect of La^{3+} substitution on the structural and thermoelectric properties of $Ca_{3-x}La_xCo_4O_{9+\delta}$, J. Eur. Ceram. Soc. 39 (2019) 3320-3326.

[60] T.R. Ming, Z.T. Shu, C.D. Wei, R. Donelson, T. Li, S. Li, Enhancement of high temperature thermoelectric performance in Bi, Fe co-doped layered oxide-based material $Ca_3Co_4O_{9+\delta}$, J. Alloys Compd. 615 (2014) 311-315.

[61] F.A. D. Srivastava, R. Freer, E. Combe, R. Funahashi, D.M. Kepaptsoglou, Q.M. Ramasse, M. Molinari, S.R. Yeandel, J.D. Baran, Crystal structure and thermoelectric properties of Sr–Mo substituted $CaMnO_3$: a combined experimental and computational study, J. Mater. Chem. C 3 (2015) 12245-12259.

Graphical abstract:

Carrier concentration optimization and chemical bond engineering lead to synergistically enhanced thermoelctric properties of $Ca_{1-x-y}La_xSr_yMnO_3$.
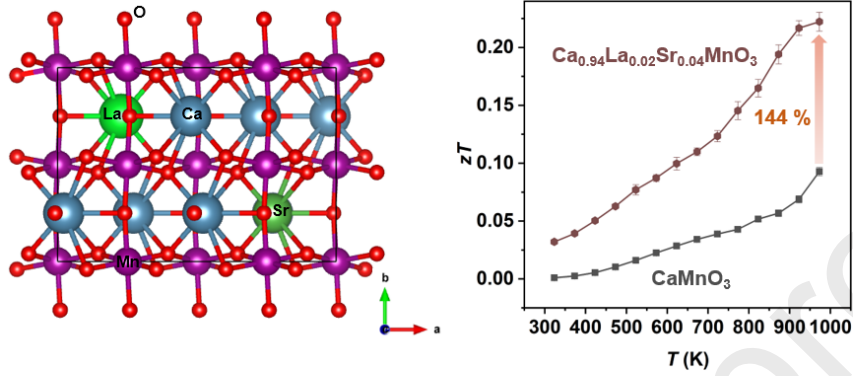
Highlights

(1) Expounding the underlying mechanism of decoupling the thermoelectric parameters of $CaMnO_3$ *via* La/Sr dual doping.

(2) Achieving carrier concentration optimization and chemical bond engineering of $CaMnO_3$ *via* a facile and well-controlled approach.

(3) Obtaining a 144% enhanced *zT* in $Ca_{0.94}La_{0.02}Sr_{0.04}MnO_3$ compared to pristine $CaMnO_3$.

Highlights